



# Deep intra-slab rupture and mechanism transition of the 2024 $M_w$ 7.4 Calama earthquake

Received: 28 February 2025

Accepted: 15 August 2025

Published online: 30 August 2025

Check for updates

Zhe Jia<sup>1</sup>✉, Wei Mao<sup>2,3</sup>, María Constanza Flores<sup>1,4,5</sup>, Sebastián Barra<sup>1,6</sup>, Sergio Ruiz<sup>4</sup>, Bertrand Potin<sup>1,4</sup>, Thorsten W. Becker<sup>1,7,8</sup>, Marcos Moreno<sup>1,9</sup>, Juan Carlos Baez<sup>6</sup>, Daniel Ceroni<sup>1</sup> & Leoncio Cabrera<sup>1,9</sup>

While subduction zone hazard is dominated by the megathrust, intermediate-depth (70–300 km) earthquakes within the slab can likewise have catastrophic impacts. Their physics remains enigmatic, with suggested mechanisms including dehydration embrittlement and thermal runaway. Here, we investigate the 2024 Chile,  $M_w$  7.4 intermediate-depth earthquake and compare the rupture extent with temperature conditions from thermo-mechanical models. We record regional geodetic co-seismic deformation and high-resolution seismicity associated with this type of event. Our analyses reveal a complex rupture spanning an exceptional depth range, with distinct asperities propagating deep into the subducting lithosphere. Comparison with thermal models shows that while the rupture initiated within the cold slab core, it extended well beyond the ~650 °C isotherm that typically delineates the boundary for efficient serpentine dehydration. We suggest that the rupture likely initiated with dehydration embrittlement within the cold core but then propagated into the warmer regions through shear thermal runaway. This implies a transition of mechanisms that facilitates large-scale rupture and activates typically aseismic, high-temperature slab regions. Our findings highlight the importance of considering interactions between rupture mechanisms as well as slab thermal and compositional settings to better understand the processes governing intermediate-depth earthquakes.

Most earthquakes occur along subduction zones at convergent plate boundaries, where tectonic plates collide and one plate sinks beneath another. Among these events, intermediate-depth earthquakes are defined as those occurring between 70 and 300 km depth range<sup>1,2</sup>. Although intermediate-depth earthquakes generally pose lower seismic hazard than shallower events, these events can

still produce destructive ground accelerations<sup>3,4</sup>, potentially resulting in substantial fatalities and extensive economic losses<sup>5</sup>. An example is the  $M_w$  7.8 1939 Chillán intermediate-depth earthquake<sup>6</sup>, which tragically led to a larger loss of life in Chile than any of the megathrust events on record. An improved understanding of the rupture behavior and maximum magnitude of

<sup>1</sup>Institute for Geophysics, Jackson School of Geosciences, UT Austin, Austin, USA. <sup>2</sup>State Key Laboratory of Earth System Numerical Modeling and Application, College of Earth and Planetary Sciences, University of Chinese Academy of Sciences, Beijing, China. <sup>3</sup>Seismological Laboratory, California Institute of Technology, Pasadena, CA, USA. <sup>4</sup>Department of Geophysics, Universidad de Chile, Santiago, Chile. <sup>5</sup>Department of Geology, Universidad de Chile, Santiago, Chile. <sup>6</sup>National Seismological Center, Universidad de Chile, Santiago, Chile. <sup>7</sup>Department of Earth and Planetary Sciences, Jackson School of Geosciences, UT Austin, Austin, TX, USA. <sup>8</sup>Oden Institute for Computational Engineering & Sciences, UT Austin, Austin, TX, USA. <sup>9</sup>Department of Structural and Geotechnical Engineering, Pontificia Universidad Católica de Chile, Santiago, Chile. ✉e-mail: [zjia@ig.utexas.edu](mailto:zjia@ig.utexas.edu)

intermediate-depth earthquakes is thus imperative for seismic hazard assessment.

For most subduction zones, intermediate-depth seismicity forms upper and lower (double) seismic planes inside the slab<sup>7–9</sup>. To explain the stresses in these planes, forces including slab pull<sup>10</sup> and the flexure of the subducted lithosphere<sup>11</sup> have been proposed, where unbending of slabs can lead to downdip compressional and tensional stress within the upper and lower plane, respectively. However, given that the pressure and temperature at intermediate-depths exceed those typical of the brittle-ductile transition<sup>12</sup>, the physical mechanism for shear faulting remains unclear. There are two major hypotheses: the embrittlement of rock caused by slab dehydration, where water released from the subducting plate increases fluid pressure and causes the surrounding rock to fracture<sup>1,13</sup>, and thermal runaway, an instability where shear heating softens rock, creating a feedback loop of focused strain that culminates in rapid slip<sup>14,15</sup>. Observational efforts to test these hypotheses have typically focused on seismicity distributions<sup>9,16,17</sup>, whereas studies examining rupture properties have revealed characteristics including relatively high stress drops, fast rupture velocities, and a systematic decrease in aftershock productivity with increasing depth, which may be influenced by slab dehydration<sup>18–20</sup>. However, the rupture extent of large intermediate-depth earthquakes, their local temperature and mineral compositions, and their interaction with the double seismic zone, remain poorly constrained. This limits our capability to test the physical boundaries of the proposed source mechanisms including dehydration embrittlement and thermal runaway.

On July 19, 2024, an earthquake of  $M_w$  7.4 struck Northern Chile near Calama, named here the 2024 Calama earthquake. This event occurred within the oceanic lithosphere where the Nazca plate subducts beneath South America. In the region, other similarly large intraplate, intermediate-depth events have been reported, the  $M_w$  8.0 Calama 1950 and  $M_w$  7.8 Tarapacá 2005 events (Fig. 1)<sup>6</sup>. The 1950 earthquake occurred almost at the same longitude but a few tens km to the South from Calama 2024 (Fig. 1), albeit with location uncertainty of 50–100 km<sup>21</sup>. Its rupture was constrained by analog teleseismic data

only, indicating a normal faulting focal mechanism with poor constraints on rupture dynamics<sup>21</sup>. The 2005 Tarapacá event occurred further north with a subhorizontal rupture<sup>19,22,23</sup>. Cabrera et al.<sup>20</sup> noted that deeper events located at elevated temperatures present relatively fewer aftershocks but some other studies<sup>24,25</sup> did not find this pattern.

At a similar latitude as the 2024 Calama earthquake, several well-recorded events of magnitudes below 7, including the 2007  $M_w$  6.7 and 2020  $M_w$  6.9 earthquakes, occurred within the 300°–400 °C isotherms in the oceanic crust and upper lithospheric mantle (Fig. 1)<sup>26,27</sup>. This pattern suggests a role of slab thermal structure in confining ruptures. However, the 2024 Calama event, with its significantly larger magnitude, likely involved a more spatially extensive rupture and fault geometry than previous earthquakes. Hence, it provides a unique opportunity to investigate intermediate-depth earthquakes, providing an important probe of the thermodynamic regime. For example, the thermal state of the slab, which affects mineral phase transitions, plays a critical role in determining whether dehydration embrittlement is feasible, thus influencing rupture processes.

In this work, we perform a comprehensive investigation of the rupture process, aftershock sequence, and thermal environment for the 2024  $M_w$  7.4 Calama earthquake. We use a range of seismic data, including accelerograms and seismograms from a dense local network, along with teleseismic recordings (Fig. 1 and supplementary Fig. S1), to constrain the spatiotemporal evolution of the event. Additionally, we use coseismic displacement from continuous GNSS data (Fig. 1) to invert for the final static slip distribution. Our results reveal that the 2024 event ruptured multiple asperities along a steeply dipping fault plane, extending across an unexpectedly large depth range of over ~50 km. This implies that the rupture might have reached beyond the cold core of the slab. Comparison with geodynamic models indicates that the rupture indeed extended beyond the region where conditions are favorable for efficient serpentine dehydration. These observations suggest a possible rupture transition from dehydration embrittlement to shear thermal runaway for large intermediate-depth earthquakes.

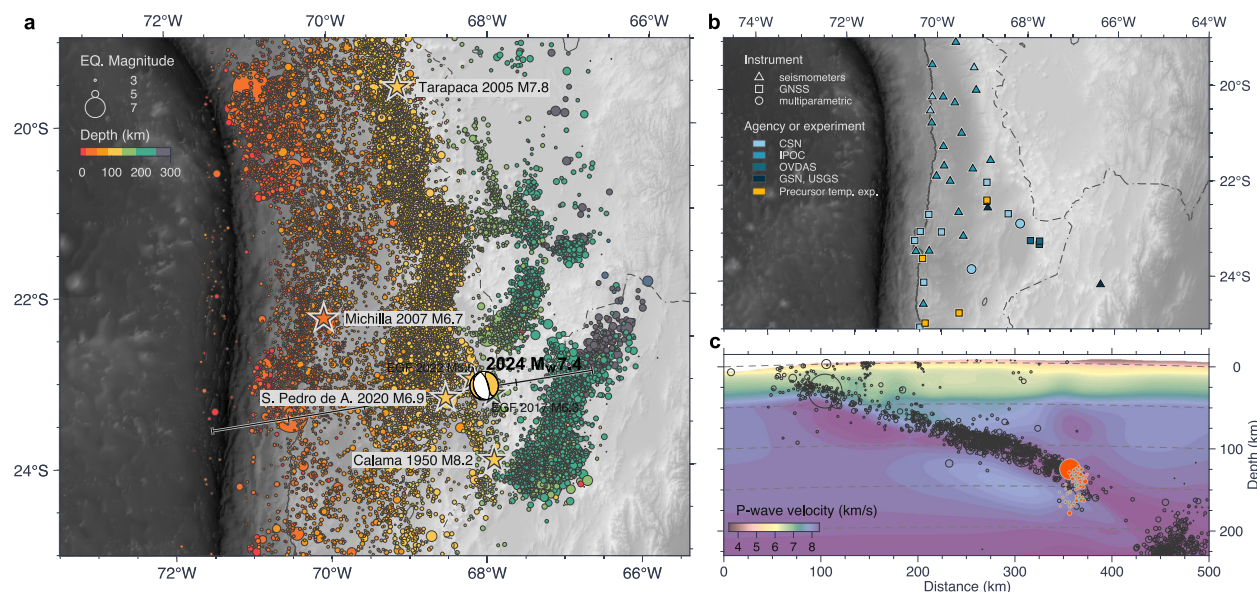


**Fig. 1 | Tectonic setting and seismicity in northern Chile.** **a** Map of seismicity in Northern Chile, based on the relocated catalog of Potin et al.<sup>31</sup>. The largest historical events in the region, and the two used empirical Green's function events, are marked with stars. The beachball shows the Global CMT solution (<https://globalcmt.org>) of the 2024  $M_w$  7.4 Calama earthquake. **b** Distribution of seismic and

geodetic stations used in this study. **c** Cross-section along the profile shown in (a), red circles are aftershocks relocated in this work. Black circles represent background seismicity within 25 km of the cross-section plane, and orange circles indicate the  $M_w$  7.4 mainshock and its aftershock sequence. Background seismic tomography is from Potin et al.<sup>31</sup>.

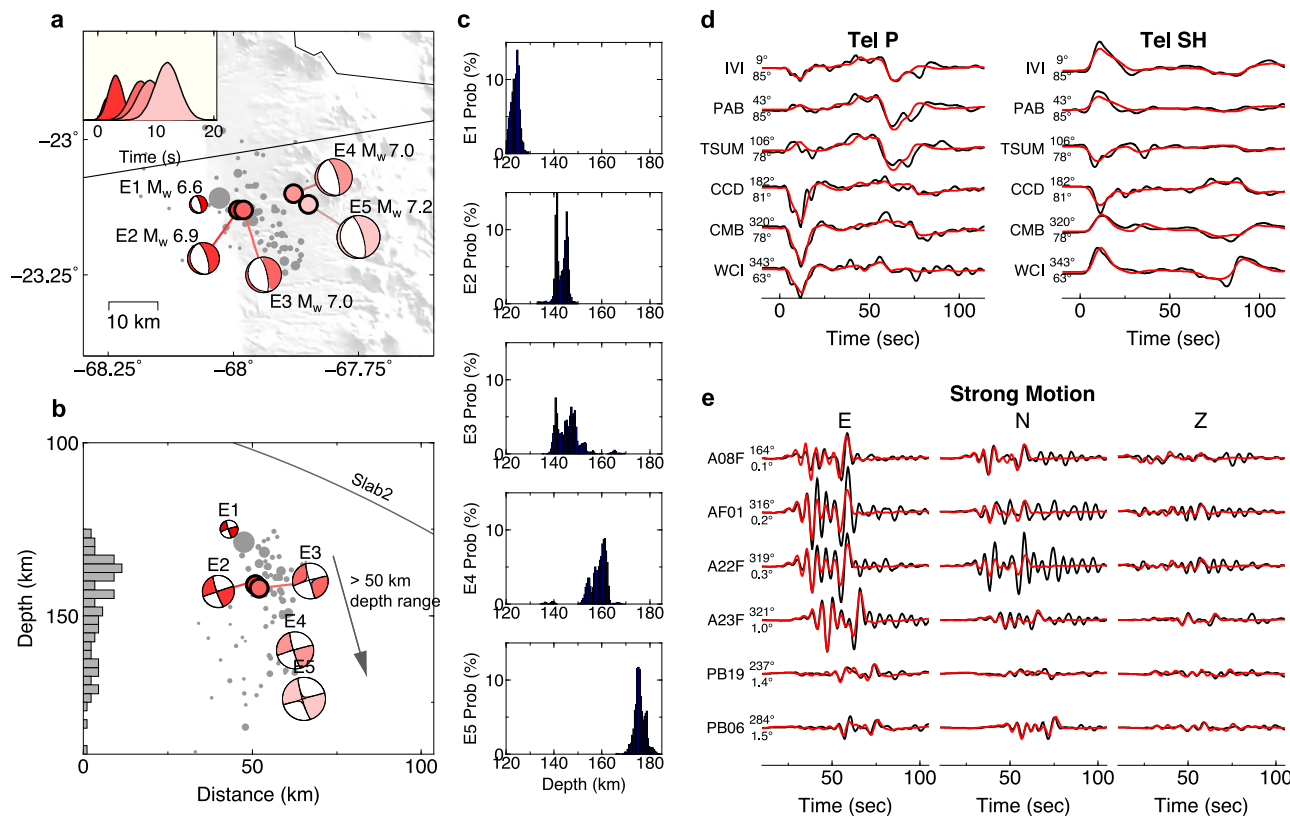


**Fig. 2 | Rupture process of the 2024 Calama  $M_w$  7.4 event.** **a** Subevent locations and focal mechanisms (red beach balls). The hypocenter is collocated with the first subevent E1. The aftershocks detected by Chile Seismic Network (CSN) are displayed by the gray dots in the background. The inset box shows the moment rate functions for all subevents. **b** Cross section along the profile in (a) showing the subevents propagated sub-vertically, consistent with the aftershock locations (gray

dots), favoring the steep down-dip plane dipping eastward. The top black solid line indicates the slab surface from Slab2<sup>41</sup>. Histogram shows the density of aftershocks as a function of depth. **c–e** Representative data (black) and synthetic (red) waveform fits for teleseismic *P* and *SH* waves (0.005–0.2 Hz), and regional strong motion (0.02–0.2 Hz) full waves. The numbers leading the traces are azimuths and distances.

## Results

### Subevent characterization of the rupture process

Local strong motion data and teleseismic waveforms show a complex pattern of *P* and *S* waves indicative of rupture of different sub-sources for the 2024 Calama event (supplementary Fig. S2). This motivates a subevent inversion for the spatiotemporal rupture process of the  $M_w$  7.4 earthquake based on teleseismic *P* and *SH* waves from 54 global seismic stations and regional full waveforms from 47 strong motion stations (supplementary Fig. S1). Our method partitions complex rupture observations into a series of simpler point source subevents with their own timing, location, source duration, and moment tensors<sup>28–30</sup>. A nonlinear inversion is implemented by Markov Chain Monte Carlo sampling, and we iteratively increase the number of subevents until the waveforms are fit sufficiently well (See the Methods section for more details). Locations and moment tensors of subevents are free parameters and provide information on fault geometries when those are not otherwise constrained.

We find that the 2024 Calama  $M_w$  7.4 earthquake can be best modeled with five distinct subevents, where the best-fit subevent number is optimized based on the trade-off between waveform misfit and model complexity (Supplementary Fig. S3). In particular, a 5-subevent model provides noticeably better fits to complex waveform features compared to models with fewer subevents (Supplementary Fig. S3). The five subevents span over ~20 s, with an eastward progression over a horizontal distance of ~25 km (Fig. 2a). In contrast, the vertical extent of the rupture is much larger, with the subevents spanning a depth range of ~50 km (Fig. 2b). The rupture progression initiated with a  $M_w$  6.6 subevent centered at 125 km depth (E1), close to

our relocated hypocenter at 128 km. The rupture then triggered deeper subevents E2 ( $M_w$  6.9) and E3 ( $M_w$  7.0), which are close, slightly east of E1 but at a larger depth of 142 km. As the rupture advances, subevents E4 ( $M_w$  7.0) and E5 ( $M_w$  7.2) occurred even deeper, with centroids at 160 km and 174 km, respectively. Waveform fits (Fig. 2d, supplementary Figs. S4, S5) and model uncertainties (Fig. 2c, supplementary Fig. S6) indicate that the source parameters for each subevent are well resolved. The wide, asymmetric duration distributions for later subevent parameters (supplementary Fig. S6), as truncated by the limits of the search algorithm, indicate that their durations are not tightly constrained with long-period data. However, subevent timings and locations are well constrained. Given that the rupture may have initiated at depths shallower than the centroid of E1 and extended to depths larger than the centroid of E5, the whole depth range ruptured by the  $M_w$  7.4 earthquake likely exceeded 50 km.

The compact horizontal yet substantial vertical extent of the subevents suggests that the rupture propagated along a steeply eastward-dipping fault plane. This geometry aligns well with the steep nodal plane of the subevent moment tensors (Fig. 2b). We also relocated the aftershocks for 2024 Calama event by manually identifying the *P* and *S* phases of seismograms recorded at local seismic stations for all aftershocks reported by the Chilean Seismic Network (CSN) using a 3D velocity model<sup>31</sup>; results are shown in Figs. 1c, 2c, and supplementary data 1. Our detected and relocated aftershock seismicity indicates an eastward-dipping band spanning depths of 120–180 km, which closely matches the subevent hypocenters (Fig. 2b). The early, shallow subevents E1–E2 account for only 20% of the total moment release but are associated with high aftershock density. In contrast, the

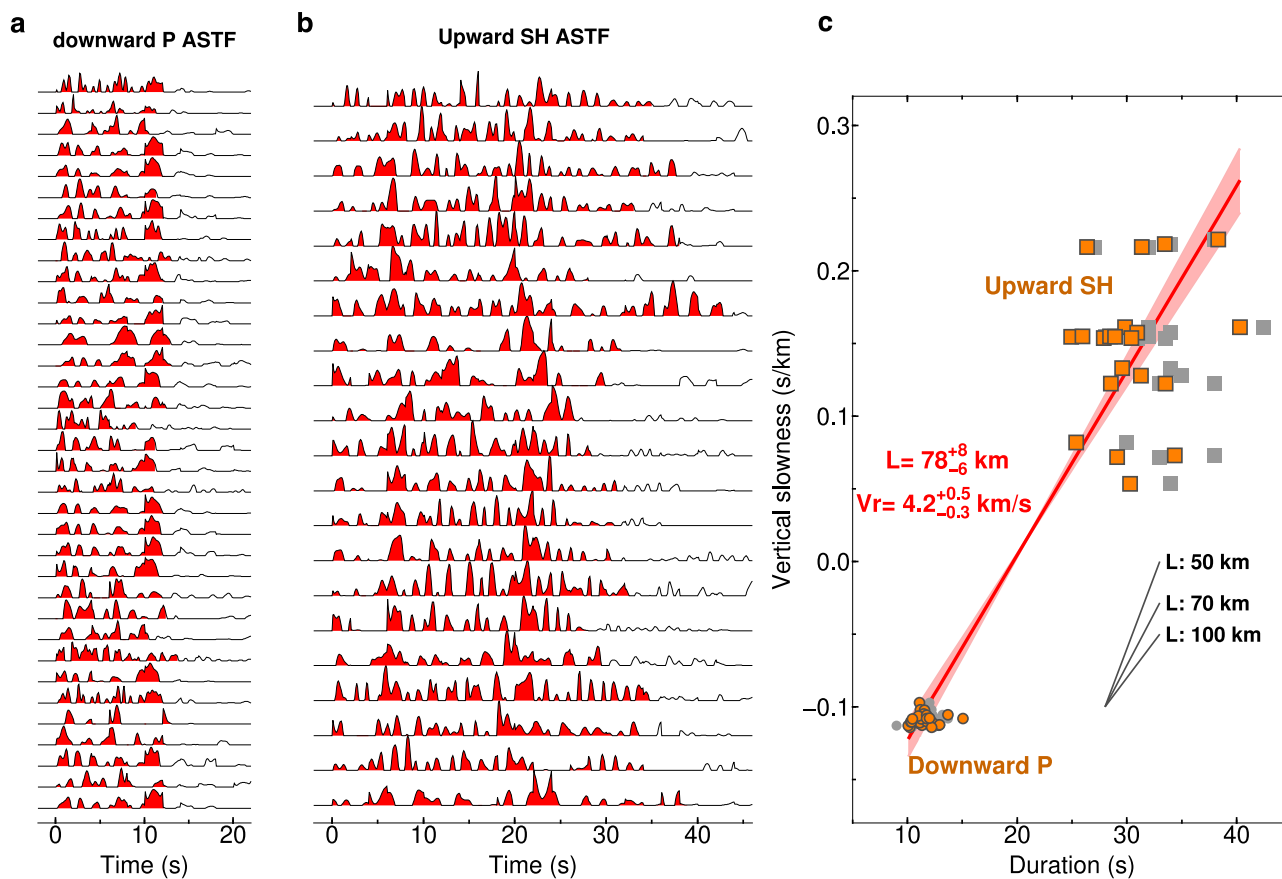


**Fig. 3 | Determination of rupture extent and velocity using source time function deconvolution.** **a** Downward apparent source time functions (ASTFs) deconvolved from downgoing teleseismic  $P$  waves. The waveforms of the target event and EGFs are filtered between 0.02–0.2 Hz. STF durations are defined by the red shading which contains most of the energy. **b** Upward ASTFs deconvolved from upgoing regional  $SH$  waves. The waveforms of the target event and EGFs are filtered between 0.03–1 Hz. **c** Inversion for the rupture extent and velocity. Gray and

orange squares indicate the apparent source durations as a function of the vertical slowness, before and after the horizontal rupture directivity correction, respectively. The orange line indicates a linear fit to the observed trend, corresponding to a rupture length of 78 km and rupture velocity of 4.2 km/s. The surrounding-colored area illustrates the 95% confidence limit of the slope, corresponding to the error range of the resolved rupture parameters. The black lines indicate the slopes for rupture lengths of 50, 70, and 100 km, respectively.

later, deeper subevents (E3–E5) contribute the bulk (80%) of the seismic moment, yet have lower aftershock density and more scattered aftershock distributions (see histogram in Fig. 2b). This suggests a more complete stress drop in the larger asperities ruptured during the later stages of the earthquake, given that the larger seismic moment over a compact rupture area implies a higher stress release. This interpretation is supported by the depletion of aftershocks for the later rupture stage, as a thermally driven comprehensive rupture would leave minimal residual stress to trigger aftershocks.

#### Validation of the fault geometry and rupture extent

To further validate the rupture characteristics and depth extent for the 2024 Calama, we conducted directivity analysis on the broadband recordings. If there were no vertical rupture propagation, the apparent duration of both downgoing and upgoing body waves would be identical, i.e., no Doppler effect. However, for a unilaterally propagating rupture along dip, we expect a directivity effect: shorter and longer duration in the direction of rupture and opposite to it, respectively. To constrain source durations, we use two local earthquakes, the 2017/04/15  $M_w$  6.2 and 2022/12/10  $M_w$  5.6, to generate empirical Green's functions (EGFs)<sup>32,33</sup> (Fig. 1a), and deconvolve the downgoing  $P$  and upgoing  $SH$  waves for the shared regional and global seismic stations for the apparent source time functions (STFs)<sup>34,35</sup>. Since the smaller events have similar depth and focal mechanisms, the derived EGFs allow removal of the shared path and site effects.

Following deconvolution, we correct the stretching on the apparent source duration caused by the horizontal rupture toward the east as inferred from the subevent model. We then invert for the rupture dimension and velocity through regression, as those are linear functions of the vertical slowness and the corrected source durations for each station and phase<sup>36–38</sup>.

The apparent STFs for downgoing  $P$  and upgoing  $SH$  waves have distinct durations and shapes (Fig. 3). Convolved with EGFs, they provide excellent fits to the observed waveforms of the Calama earthquake (Supplementary Figs. S7–S10). The downgoing STFs show coherent phases that align with the five subevents determined from the waveform inversion, with total duration of ~12–13 s (Fig. 3a). In contrast, the upgoing STFs have much longer durations of ~30 s, which suggests pronounced downward rupture directivity (Fig. 3b). The upgoing STFs also contain over 10 pulses, which reflect smaller scale asperities superimposed on the 5 major, lower frequency subevents ruptured coseismically (Fig. 3b). These details are preserved along the shorter travel distance and less-attenuating upgoing path, whereas the long teleseismic path for the downgoing waves acts as a low-pass filter. Applying a low-pass filter below 0.4 Hz to the upgoing STFs reveals comparable longer period subevent pattern (Supplementary Fig. S11). Meanwhile, the temporal gaps in the upgoing source time functions are necessitated by the waveform data in the deconvolution (Supplementary Fig. S12). Therefore, we interpret these high-frequency asperities as real, resolvable features of the rupture. Our regression analysis

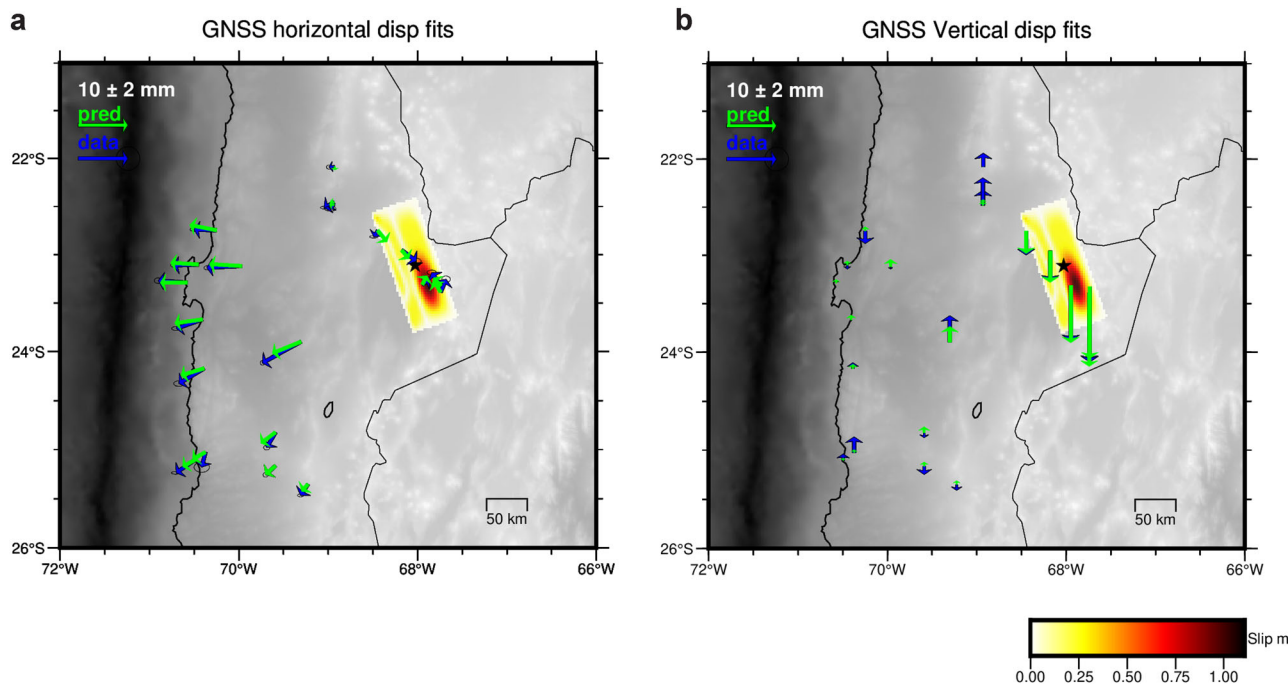


**Fig. 4 | Geodetic constraints on the fault geometry and slip distribution.**

a Coseismic slip distribution and GNSS horizontal displacement fits for the sub-vertical fault plane. Blue and green arrows indicate observed and model-predicted displacements, respectively. b Coseismic slip distribution and GNSS vertical

displacement fits for the rupture along the sub-vertical fault plane. Full fits to both vertical and horizontal component displacements for the two fault planes are shown in supplementary Figs. S17, S18.

on the observed STF durations yields an optimal rupture length of 78 km and average velocity of 4.2 km/s, along a fault plane with 71° eastward dip. This angle coincides with the average dip of the 5 subevents' steeper fault planes. Moreover, the large downdip rupture dimension aligns with the depth range of the subevents and aftershocks (120–180 km) and explains the anomalously broad teleseismic *sP* and *sS* depth phases (supplementary Fig. S4). Our relocated aftershock distribution aligns well with the sub-vertical plane inferred from the subevents (Fig. 2). We also searched for precursor events and further aftershocks using template matching. No precursors were observed and the aftershock productivity is high compared to other similar events in the area<sup>20</sup> (supplementary Figs. S13, S14).

The mainshock produced horizontal displacements of ~1 cm extending more than 250 km from the epicenter and a subsidence of ~20 cm above the rupture. Using these GNSS-derived displacements, we estimated the geodetic co-seismic slip distribution (Fig. 4). We tested both the sub-horizontal and sub-vertical planes based on the focal mechanism and our proposed hypocenter (Supplementary Fig. S15). Acknowledging the inherent challenge of resolving fault geometry and the detailed slip distribution for such a deep source, we found that both planes can fit the GNSS observations (supplementary Figs. S16–S18). However, the fit for the vertical plane model is slightly better and has relatively smoother inferred coseismic slip. The insignificant misfit differences suggest that geodetic data may not tightly constrain fault geometry. Nonetheless, the effective slip distribution for the sub-vertical plane is consistent with our subevent inversion, directivity analysis, and aftershock patterns. In conjunction, these provide much stronger seismological constraints on the rupture geometry.

#### Rupture across the dehydration isotherm suggests a mechanism transition

The large depth extent of the 2024 Calama event renders it an important probe for understanding the mechanisms of intermediate-depth earthquakes in general. The event likely ruptured a substantial

portion, if not reached the base of the subducting lithosphere. This is further supported by the distinct character of later waveform arrivals in the strong motion data, which necessitates deep depths of subevents E4–E5, as indicated by our forward modeling tests (Supplementary Fig. S19). The rupture could extend well beyond the inferred 600 °C to 650 °C isotherm at depths of 120–180 km, which bound the region capable of hosting dehydration embrittlement<sup>13,39</sup>, a key mechanism invoked to explain the intermediate-depth seismicity in northern Chile<sup>17</sup>. Compared with other intraplate earthquakes<sup>20</sup>, 2024 Calama had a significant number of aftershocks, which suggests that at least part of its rupture occurred in a colder, brittle regime. This is more analogous to shallower events such as the 2007 Michilla M<sub>w</sub> 6.7 and 2020 Calama M<sub>w</sub> 6.9 earthquakes<sup>26</sup>, rather than events in high-temperature zones (>600 °C) where aftershocks are typically suppressed.

We further assess the temperature environment of the region by computing steady-state, semi-kinematic thermal geodynamic models for the subduction zone along a 2D cross section<sup>40</sup>. The slab geometry is constrained by multiple independent datasets, including regional seismicity, seismic tomography, and the latest high-resolution CSN earthquake catalog<sup>31,41</sup>. Our models also incorporate the incoming plate thermal structure inferred from plate age, and an adiabatic temperature gradient (see Methods section). As for all such models, isotherms are strongly affected by plate age and convergence rate, the product of which is a scaled Peclet number, the “thermal parameter”; it determines how deep cold isotherms are subducted before they diffuse away. Our results indicate that although the M<sub>w</sub> 7.4 earthquake likely nucleated near the cold core of the slab, its ~78 km downdip rupture extended far beyond the 650 °C isotherm that bounds the zone where serpentine can efficiently dehydrate to olivine (Fig. 5). This finding is robust to variations in thermal modeling setups and other methodological choices. Adopting alternative slab geometries (e.g., Slab2<sup>41</sup>) or varying slab age still implies that 2024 Calama ruptured beyond the serpentinite dehydration isotherm (Supplementary Fig. S20). Even under the alternative hypothesis that the slab resides

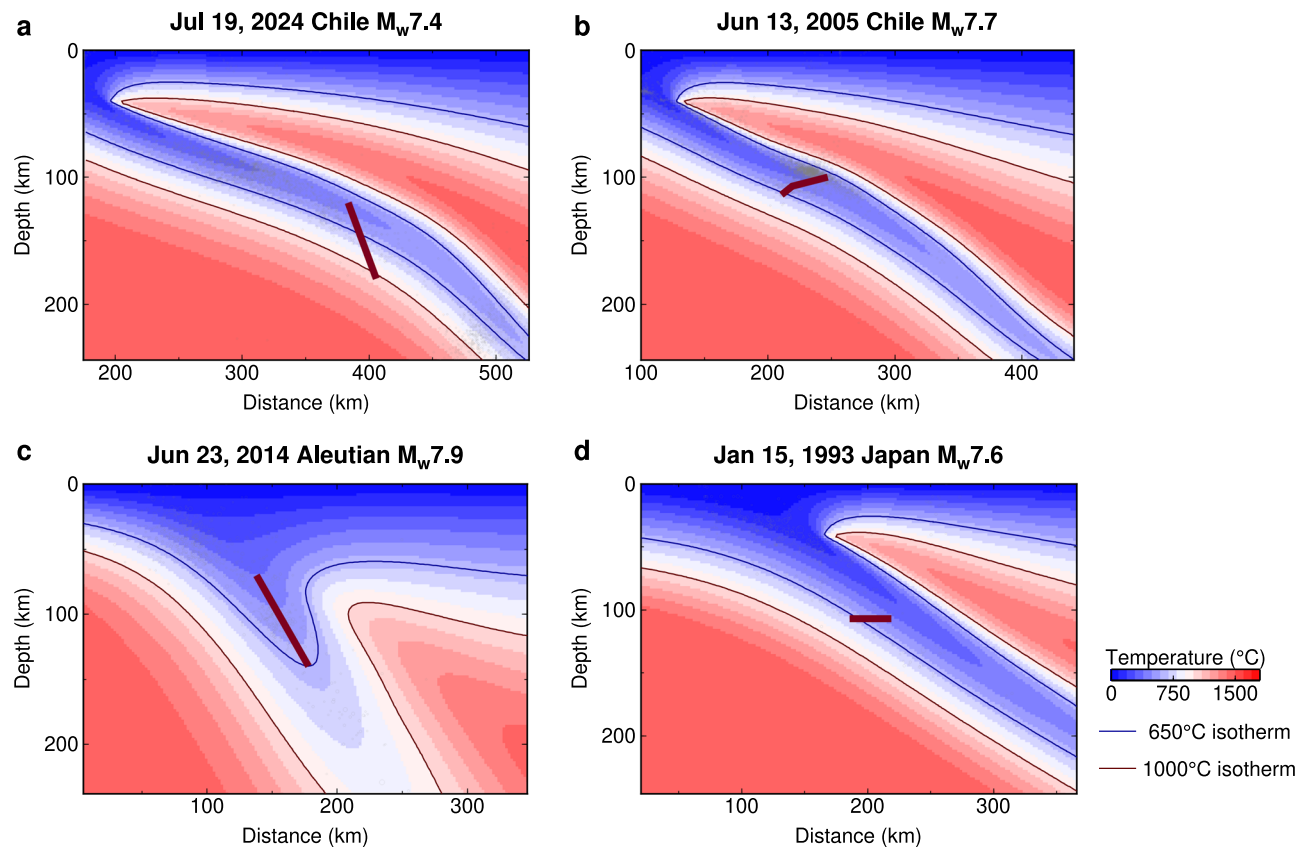


**Fig. 5 | Thermal environment of the 2024 Calama earthquake rupture.** This figure compares the rupture extents and thermal environments for **a** the 2024 Chile  $M_w$  7.4 earthquake with **b–d** other historical large intermediate-depth earthquakes. The color shows temperature derived from thermodynamic simulations along cross sections shown in Table S3. The dark red lines indicate the estimated rupture

extent for the 2024 Chile  $M_w$  7.4 (this study), 2005 Chile  $M_w$  7.7<sup>22</sup>, 2014 Aleutian  $M_w$  7.9<sup>4</sup>, and 1993 Japan  $M_w$  7.6<sup>50</sup>, respectively. The thin blue and red lines are the 650 °C and 1000 °C isotherms, respectively. Background gray circles indicate the seismicity from the NEIC catalog since 2000.

deeper, the thickness of its cold core is still well constrained. Meanwhile, our thermal model is consistent with other thermal models for the wider region<sup>42,43</sup>; those also feature a cold core too thin to contain the entire Calama rupture (Supplementary Fig. S21). Note that other hydrous minerals such as chlorite, talc, and amphiboles can also dehydrate under varying pressure-temperature conditions<sup>44–46</sup>. However, most amphiboles dehydrate at lower temperatures and thus release fluids at shallower depths, while chlorite and talc are present in substantially lower abundances than serpentine<sup>13,45</sup>. As a result, antigorite serpentine remains the dominant contributor to fluid release and large-scale faulting. Therefore, once the rupture extended beyond into warmer regions, mechanisms other than dehydration embrittlement likely governed further rupture propagation.

We suggest that the rupture likely transitioned into thermal runaway, involving localized shear heating that weakens the rock and sustains rupture propagation. Thermal runaway alone is unlikely to be a general mechanism for earthquakes, due to the lack of a spontaneous self-localization<sup>14,15</sup>. However, slow deformation over geological time scales allows significant strain to accumulate. Once a triggering mechanism like dehydration embrittlement can initiate localized failure, shear thermal runaway, even at high temperatures, can act as a positive feedback loop of shear heating that may substantially weaken the fault, generating large slip asperities, and as a consequence more complete moment release<sup>47–49</sup>. Our observations agree with such a transition: the second rupture stage occurs at depths with sparse historical seismicity and low aftershock density (Fig. 1), yet releases 80% of the total seismic moment (E3-E5) (Fig. 2). This suggests that a secondary mechanism such as shear thermal runaway can play a critical

role for fault weakening at larger depths, including for intermediate-depth earthquakes.

## Discussion

Hypotheses for intermediate-depth earthquakes typically focus on seismicity concentrated within the cold core of the slab, where dehydration embrittlement is considered dominant, and transitions from dehydration embrittlement to other mechanisms, such as thermal runaway, are rarely observed. Among historical  $M_w > 7.5$  intermediate-depth events, the 1993  $M_w$  7.6 Kushiro-oki, the 2005  $M_w$  7.7 Tarapacá, and the 2014  $M_w$  7.9 Rat Island earthquakes are the few that have well-defined fault planes and along-dip rupture extent<sup>4,22,23,50</sup>. In analogy to our Calama models, we estimate the temperature environment for those other intermediate-depth earthquakes (Fig. 5). All three comparables have rupture areas generally confined to the cold slab core, below the 650 °C serpentine dehydration isotherm, where dehydration of gabbro and basalt occurs within the slab, facilitating potential brittle deformation. 2024 Calama event does present a striking exception where the rupture extends into substantially warmer regions, perhaps up to 1000 °C. This inference is robust with respect to oceanic plate age variations (supplementary Fig. S20).

A potential contributing tectonic factor for Calama is the high degree of megathrust coupling<sup>51</sup>, which may enhance slab pull forces and impose additional stress on the downgoing slab. This loading, combined with the slab's thermal structure, may facilitate a transition from dehydration embrittlement to shear thermal instability, enabling failure beyond the cold slab core. Our findings complement earlier suggestions that thermal runaway, where localized heating from shear

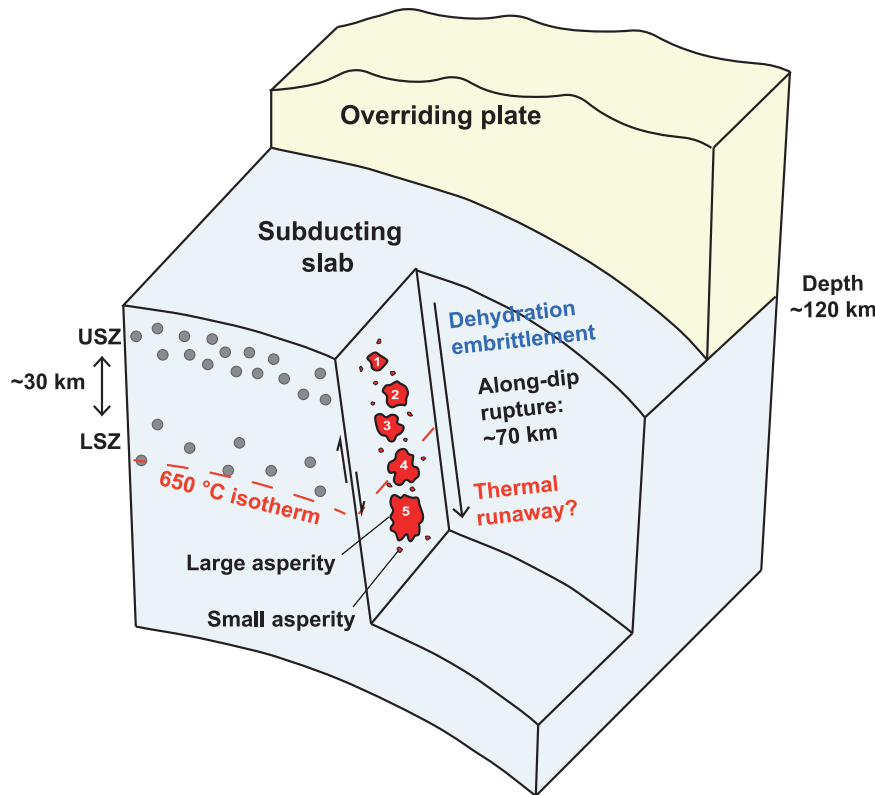


**Fig. 6 | Summary schematic of the intraslab rupture and mechanism transition for the  $M_w$  7.4 event.** The earthquake ruptured seismic asperities of various scales (red polygons), and penetrated through the 650 °C boundary allowable for

serpentine dehydration, which suggests transitioning to another mechanism, likely shear thermal runaway. Gray dots represent seismicity that delineates the upper and lower seismic zones.

stress reduces resistance and facilitates rapid slip, may occur for moderate-size intermediate-depth events<sup>52,53</sup>. We demonstrate that such a mechanism may also operate in large-scale intermediate-depth ruptures.

A similar transition from mineral phase change-driven to shear heating-accommodated rupture has also been proposed for deeper earthquakes (300–700 km), such as for 1994 Bolivia, 2013 Okhotsk, and 2018 Fiji earthquakes<sup>28,48,54</sup>. For both depth ranges, the slab's thermal structure appears to be the common control governing the mechanism transitions from the colder core to the warmer slab halo. These temperature patterns influence phase changes and associated weakening processes, albeit through distinct mechanisms. For intermediate-depth earthquakes like the 2024 Calama event, the initial trigger is the dehydration of the hydrous minerals such as serpentine and similar hydrous minerals in the cold slab core (Fig. 6). In contrast, for the deep earthquakes, the transformational faulting of metastable olivine is likely the first driver<sup>12,48,54</sup>. Despite the different initial triggers, both settings involve thermal runaway as the subsequent mechanism that allows the rupture to propagate further, into hotter, otherwise ductile regions. However, the details governing these transitions, potentially involving factors including compositional and grain size variations affecting stress state, frictional properties, and variations in hydration status, remain to be further investigated.

Besides its remarkably large effective fault plane, 2024 Calama also ruptured at a relatively fast velocity exceeding ~93% of the local shear wave velocity ( $V_S$ ). This is above the typical rupture speeds for large intermediate-depth earthquakes, usually in the range of 0.2–0.8 of  $V_S$ <sup>23,55–57</sup>. While methods that analyze far-field Mach cones in surface waves are effective for constraining horizontal supershear<sup>58,59</sup>, for Calama 2024, which primarily propagated down-dip, body-wave analysis on Doppler-like compression of source durations provides the most robust constraint on rupture velocity. Rupture speeds at ~0.9  $V_S$

fall in the “forbidden zone” between Rayleigh and shear wave speeds, where the rupture is theoretically unsustainable as the fault generates rather than absorbs strain energy<sup>60–62</sup>. Hence, it is likely that the inferred rupture velocity of 2024 Calama is an average of mixed rupture, including both regular subshear and episodic supershear propagation. This inference is consistent with the subevents and deconvolved source time functions (Figs. 2, 3), where the rupture is characterized by a series of distinct pulses, suggesting propagation through a heterogeneous field of asperities (Fig. 6).

We attribute the inferred, episodic supershear speeds to the triggering of these asperities, where dynamic stress perturbations from seismic waves initiate failure on the nearby faults. Dynamic triggering has been widely observed for smaller earthquakes triggered by distant large events<sup>63–65</sup>, and has been suggested to generate deep earthquakes in the warmer regions of the slabs<sup>49,66</sup>. However, the complex rupture behavior we observed for the Calama earthquake, characterized by distinct source time function pulses that suggest sequential activation of multiple asperities during the rupture, has rarely been documented for intermediate-depth events.

Asperities likely reflect compositional and structural heterogeneities along the fault, and they can play a critical role in modulating rupture dynamics<sup>62,67–69</sup>. For intermediate-depth events such as 2024 Calama, asperities might be loaded near critical to the background loading, such as from slab bending. Spontaneous rupture may be unlikely on the asperities in warmer and less brittle regions, but once the rupture initiates in the cold slab core, dynamic stress perturbations may activate surrounding asperities, possibly triggering thermal runaway and facilitating rupture into normally stable regions. Future work may reveal how interactions between rheological heterogeneities, thermal gradients, and stress states could potentially determine whether asperities remain quiescent or are activated during rupture in a prospective sense.

In summary, by integrating comprehensive earthquake rupture imaging using seismic and geodetic data, as well as thermomechanical modeling, our analyses on the 2024 M<sub>w</sub> 7.4 Calama earthquake reveal that the rupture spanned an unusually large depth range. A succession of subevents penetrated into the outer reaches of the slab, likely involving a transition from dehydration embrittlement in the cold core to thermal runaway in the warmer slab halo. The 2024 Calama event shows that even high-temperature regions of the slab, typically considered aseismic, can be dynamically activated during large events. Allowing for such rupture transitions substantially extends the total possible rupture area and seismic moment available. This calls for reassessing the seismic hazard when estimating maximum magnitudes for large earthquakes in subduction zones.

## Methods

### Earthquake detection using template matching

We used template matching<sup>70</sup> to detect unreported earthquakes around the 2024 Calama mainshock, by means of the Fast Matched Filter algorithm<sup>71</sup>. This was done by analyzing continuous broadband velocity waveforms of six stations of the CSN network situated near the epicenter of the mainshock and at distances of less than 3°. Following previous regional studies<sup>20,26</sup>, we used three component records downsampled to 40 Hz and bandpass filtered from 1 Hz to 20 Hz. For the application of template matching, an initial catalog is required, for which we use the seismicity reported by CSN ([www.sismologia.cl](http://www.sismologia.cl)) in space-time windows, as will be explained below. For each event of the initial catalog, P-wave and S-wave arrivals for all selected stations were calculated using a local 1-D velocity model<sup>72</sup>. To estimate the templates as well as the moveouts used in the analysis, we use the vertical component to scan the P-wave and the horizontal components to scan the S-wave<sup>71</sup>. In this sense, we cut the continuous waveforms from 2 s before the theoretical arrival times until 3 s after. Thus, we made one template waveform for each component of every station selected, which represents 5 s of the recorded events.

For every event, we scanned the continuous data by moving the templates one sample, and preserving their moveouts. At every position of the sliding windows, we calculated an averaged cross-correlation coefficient (CC) over all stations and components. In order to consider only waveforms with an acceptable signal-to-noise ratio (SNR), we excluded stations with an SNR lower than 2.0 in the vertical component; others are weighted such that the sum of all weights over the stations is unity. Lastly, we removed those templates with fewer than 4 stations with acceptable SNR on the vertical component. This resulted in a time series representing the similarity between the templates and the continuous data. We used a daily detection threshold of 15 times the median absolute deviation (MAD) of the daily time-series of averaged cross-correlation coefficients to define the potential detection of an earthquake with significantly similar waveforms to the templates, assuming they occur at the same hypocentral location as the event used for the detection.

Given the possibility of obtaining consecutive detections separated by a time of less than the template waveform's duration, we removed these consecutive detections, leaving the one with highest CC and removing the surrounding detections. The magnitudes were estimated by computing the median amplitude ratio between the waveform of the templates and the detections over the stations, assuming that a tenfold increase in amplitude corresponds to one unit increase in magnitude<sup>73</sup>.

For our analysis, we considered two cases with different spatial windows to define the initial catalogs before running template matching. The first is for comparative purposes and considers the same radius of rupture (21 km) adopted by Herrera et al.<sup>26</sup> for the 2020 Mw 6.8 Calama intraslab earthquake, and the second considers a greater radius, of 47 km, calculated using expressions proposed for another Mw 7.4 event<sup>74</sup>, based on the source radius estimated by Wells

& CopperSmith<sup>75</sup>. In this context, we make two different catalogs as follows:

For DS1, the initial catalog contains every earthquake reported by CSN that originated between one month before and one month after the mainshock, and located at a distance less than 21 km from the reported hypocenter of the mainshock. With this criterion, 33 initial events were considered, of which 32 were used as templates, and 150 were finally reported after running template matching. For DS2, the initial catalog is composed of every earthquake reported by CSN and located in a distance of less than 47 km from the location of the mainshock, in a temporal window between one month before and one month after the mainshock. In this case, 84 initial earthquakes were considered, 82 were adopted as templates, and a total of 314 final events were reported after applying template matching (supplementary Figs. S13 and S14).

### Subevent inversion for rupture process

We apply a multiple-subevent inversion method<sup>29,30</sup> to constrain the source parameters of the subevents for 2024 Calama instead of kinematic finite-fault inversion, as the subevent parameterization avoids potential biases from assuming a fixed fault geometry and allows a more comprehensive exploration of the parameter space with fewer free parameters. Subevent inversion was also selected over back-projection, as our primary goal is to resolve down-dip rupture directivity, a characteristic to which back-projection is largely insensitive. The number of subevents is determined by iteratively adding subevents until the improvement in data fit becomes insignificant. Each subevent is characterized by 5 nonlinear parameters: horizontal location, depth, centroid time, and centroid duration, except for the first subevent, whose horizontal location is fixed at the CSN hypocenter to prevent simultaneous shifting of all subevent locations and seismogram timings. Additionally, each subevent has 5 linear parameters corresponding to its deviatoric moment tensor components.

The inversion employs a two-stage algorithm to efficiently explore parameter space. In the outer stage, we search for nonlinear location and timing parameters using a Metropolis-Hastings Markov Chain Monte Carlo (MCMC) sampler. During each MCMC random walk, one nonlinear parameter is perturbed while others remain fixed, which allows a high acceptance rate and sampling efficiency<sup>76</sup>. For each set of nonlinear parameters, we linearly invert the seismic data to estimate subevent moment tensors<sup>77</sup>. This separation of nonlinear and linear parameter estimation reduces computational cost and enhances efficiency.

We generate 192 MCMC chains and retain the best-performing 48 chains to mitigate the effects of bad initial samples and avoid local minima. A Bayesian framework is used in the inversion to incorporate data errors and model priors, which allows estimation of model uncertainties. Uniform prior distributions are assigned to nonlinear parameters, with horizontal location priors informed by the spatial density of early aftershocks. Although instrumental noise is minimal, we introduce a 10% empirical data error relative to misfit to account for inaccuracies in wave propagation assumptions. Model uncertainties are quantified as the 95% confidence intervals of the posterior probability density functions, defined by the 2.5 and 97.5 percentile values of the Markov Chain samples, without assuming a Gaussian fit to them.

We use P-wave displacement and velocity waveforms from 54 teleseismic stations, SH-wave displacement waveforms from 53 teleseismic stations, and three-component velocity waveforms from 47 regional strong ground motion stations. Data were obtained from the Global Seismic Network (GSN), the International Federation of Digital Seismograph Network (FDSN), and the Chilean National Seismological Center (CSN). Weights are adjusted to achieve comparable contributions to the misfit, with a weighting ratio of 3:1:0.04 for teleseismic P and SH waves, and regional data, respectively. Instrument responses and linear trends were removed, and teleseismic data were band-pass

filtered between 0.02–0.2 Hz, while regional data were filtered between 0.02–0.15 Hz. We allow time shifts of up to 2 s for teleseismic  $P$  waves, 5 s for teleseismic  $SH$  waves, and 2 s for regional data to account for path effects and picking errors. Green's functions were calculated using a local 1D velocity model<sup>72</sup> for the crust and the IAS-PEI91 model for deeper Earth structure. Teleseismic Green's functions were computed using a hybrid method combining the propagator matrix approach and ray theory<sup>78,79</sup>, while regional Green's functions were computed using the frequency-wavenumber integration method<sup>80</sup>. The optimal subevent model for the Calama event is shown in Table S1.

### Geodetic inversion of the slip distribution

We used GNSS observations from CSN (<https://doi.org/10.7914/SN/C1>), together with stations from the International GNSS Service (IGS) network<sup>81</sup> and those installed by the ANILLO-PRECURSOR<sup>82</sup> and IPOC<sup>83</sup> projects. All GNSS data were processed using the differentiation strategy<sup>84</sup>, using the Bernese 5.4 software<sup>85</sup>. The daily results were accumulated to generate time series that are compatible with the ITRF2020 reference frame<sup>86</sup>. The resulting coseismic displacements are summarized in Table S2.

Based on the earthquake focal mechanism and hypocenter location, we modeled two fault planes: (1) a sub-horizontal plane (dip = 21°, strike = 172°) and (2) a sub-vertical plane (dip = 69°, strike = 341°). We compute Green's functions for both planes using triangular elastic dislocation modeling<sup>87</sup>. We then perform a generalized least square inversion to estimate the coseismic slip distribution, where prior information is defined by the Equal Posterior Information Condition (EPIC)<sup>88</sup>. EPIC applies a spatially variable smoothing constraint based on a discrete Laplacian, which allows regions of the fault plane with dense GNSS data coverage to retain more detailed slip features while enforcing stronger smoothing in poorly constrained fault areas. We applied positivity constraints to the dip-slip components and constrained the maximum values of the slip on the strike direction. Both fault plane models achieved good fits to the GNSS data, while the vertical plane produced slightly better RMSE residuals (1.48 mm vs. 1.51 mm). Additionally, the vertical fault plane aligns more closely with the spatial distribution of observed aftershocks.

### Source time function deconvolution for rupture directivity and extent

We designed a time-domain deconvolution approach to extract the source time function from observed seismic waveforms. The problem minimizes the mismatch between the observed data  $u(t)$ , and the convolution of the source function  $s(t)$  with a predefined empirical Green's function  $G(t)$ ,

$$\min_s \|G(t)^*s(t) - u(t)\|_2^2 + \lambda \cdot L_{12}(s) \quad (1)$$

in which  $L_{12}(s)$  is a mixed  $L_1$ - $L_2$  norm regularization term to prevent overfitting of the data. The mixed norm term is defined as

$$L_{12}(s) = \sum_{g=1}^M \|s_g\|_2 \quad (2)$$

where  $s_g$  is the subvector of  $s(t)$  corresponding to group size  $g$ . Here, we choose  $g$  as 20 samples (2 s window for sampling rate of 0.1 s), and we choose  $\lambda$  as 0.05 to balance sparsity and smoothness of the resolved source time functions.

The optimization problem is solved using the CVXPY library<sup>89</sup>, with the non-negativity constraints to reflect the physical non-negativity of the source time functions.

To test the robustness of the observed gaps in the source time functions, we incorporate a second-order difference regularization to enforce smoothing in the source time function by penalizing rapid

changes in curvature,

$$\min_s \|G(t)^*s(t) - u(t)\|_2^2 + \lambda \cdot L_{12}(s) + \beta \cdot \|D_2 s\|_2^2 \quad (3)$$

where the finite-difference operator is represented as

$$\|D_2 s\|_2^2 = \sum_{i=1}^{N-2} (s_{i+2} - 2s_{i+1} + s_i)^2 \quad (4)$$

The results with  $\beta$  as 0, 10<sup>2</sup> (moderate forced smoothing), and 10<sup>4</sup> (strong forced smoothing) are shown in supplementary Fig. S12. Retrieving acceptable fits to the data requires gaps in the source time functions.

After we obtain the source time functions, we estimate the source durations for each trace. These durations are determined by identifying the main, coherent energy release that is clearly visible above noise and maintains a consistent shape across stations. We confirm its robustness by comparing our results (Fig. 3) to those derived from a standard quantitative criterion (STF amplitude  $\geq 25\%$  of the peak, used by the IRIS DMC source time function products<sup>90</sup>) (Supplementary Fig. S22). While this test results in qualitatively similar rupture parameters, the rigid threshold introduces unnatural truncations, particularly for teleseismic  $P$ -waves. Therefore, we retain our initial selections as they provide a more physically meaningful measure of source duration. These final durations are then used to correct the horizontal rupture directivity constrained from the subevent locations (25 km towards the east). We further examine the relationship between source durations and vertical slowness by fitting a linear regression model to observational data to estimate the vertical rupture directivity. The slope intercept of the regression line in Fig. 3c provides an estimate of the inverse of the vertical rupture velocity, and the  $x$ -axis intercept indicates the source duration, which allows the characterization of rupture dimension along the dip. To quantify uncertainties of the slope and the intercept, we consider two times the standard deviation errors of their respective estimates; those provide upper and lower bounds for the estimated rupture velocity and dimension, respectively.

### Thermal simulations for the slab temperatures

We conduct thermal simulations for subducting slabs at Chile, Japan, and the Aleutian subduction zones. We compute two-dimensional thermal models initialized from a plate cooling model of reference plate thickness of 95 km<sup>91</sup> based on ages of oceanic plates<sup>92</sup>, which represents the thermal state of the oceanic lithosphere at incipient subduction. For the slab surface geometry, we use a slab interface model estimated using the CSN seismicity catalog for the two northern Chile transects (Fig. 5a, b), and the slab surface from Slab2<sup>41</sup> for the other two transects (Fig. 5c, d). For the northern Chile transects, we also test the slab surface from Slab2; this does not affect our conclusions (Supplementary Fig. S21). We project convergence velocity<sup>92</sup> onto the transects (Table S3) because the plate motion velocity is not aligned with the direction perpendicular to the trench. With these initial conditions for each subducting slab, we use a finite element model to estimate the thermal structure<sup>40</sup>. These models incorporate a kinematic slab with prescribed geometry as well as a dynamic mantle wedge with a composite rheology including both diffusion and dislocation creep. The slab decouples from the overriding plate at 50-km depth. The mesh resolution is 2 km, with refinement to 1 km at the mantle wedge and slab surface. The mantle potential temperature is 1300 °C and adiabatic temperature gradient is 0.3 °C/km<sup>91,93,94</sup>. Tests assuming that the slab decouples from the overriding plate at 80-km depth show no substantial difference from the thermal simulation results used in this study.

### Data availability

All figures are plotted using GMT (<https://www.generic-mapping-tools.org/>). Seismic data are available on the IRIS Wilber 3 page (<https://ds>

[iris.edu/wilber3/find\\_stations/11455082](https://iris.edu/wilber3/find_stations/11455082)) and strong motion at <https://evtdb.csn.uchile.cl/event/030cd73d4cf743e322b7bc88f1166a4c>. GNSS observations are available at <http://gps.csn.uchile.cl>.

## Code availability

The subevent inversion code is available at <https://github.com/jiazhe868/SubMIT>, the source time function deconvolution code at [https://github.com/jiazhe868/source\\_time\\_function\\_deconvolution](https://github.com/jiazhe868/source_time_function_deconvolution), and the thermal modeling code at <https://github.com/nate-sime/mantle-convection>. Please contact the corresponding author to discuss how to use the code.

## References

- Green, H. W. & Houston, H. The mechanics of deep earthquakes. *Annu. Rev. Earth Planet. Sci.* **23**, 169–214 (1995).
- Vassiliou, M. & Hager, B. Subduction zone earthquakes and stress in slabs. *Pure Appl. Geophys.* **128**, 547–624 (1988).
- Ye, L., Lay, T. & Kanamori, H. The 23 June 2014 Mw 7.9 Rat Islands archipelago, Alaska, intermediate depth earthquake. *Geophys. Res. Lett.* **41**, 6389–6395 (2014).
- Twardzik, C. & Ji, C. The Mw7.9 2014 intraplate intermediate-depth Rat Islands earthquake and its relation to regional tectonics. *Earth Planet. Sci. Lett.* **431**, 26–35 (2015).
- Georgescu E.-S., Pomonis A. The Romanian earthquake of March 4, 1977 revisited: New insights into its territorial, economic and social impacts and their bearing on the preparedness for the future. In: *Proceedings of the 14th World Conference on Earthquake Engineering, Beijing, China*. Citeseer (2008).
- Ruiz, S. & Madariaga, R. Historical and recent large megathrust earthquakes in Chile. *Tectonophysics* **733**, 37–56 (2018).
- Hasegawa, A., Umino, N. & Takagi, A. Double-planed structure of the deep seismic zone in the northeastern Japan arc. *Tectonophysics* **47**, 43–58 (1978).
- Brudzinski, M. R., Thurber, C. H., Hacker, B. R. & Engdahl, E. R. Global prevalence of double Benioff zones. *Science* **316**, 1472–1474 (2007).
- Florez, M. & Prieto, G. Controlling factors of seismicity and geometry in double seismic zones. *Geophys. Res. Lett.* **46**, 4174–4181 (2019).
- Sleep, N. H. The double seismic zone in downgoing slabs and the viscosity of the mesosphere. *J. Geophys. Res.: Solid Earth* **84**, 4565–4571 (1979).
- Engdahl, E. & Scholz, C. A double Benioff zone beneath the central Aleutians: An unbending of the lithosphere. *Geophys. Res. Lett.* **4**, 473–476 (1977).
- Kirby, S. Interslab earthquakes and phase changes in subducting lithosphere. *Rev. Geophys.* **33**, 287–297 (1995).
- Hacker B. R., Peacock S. M., Abers G. A., Holloway S. D. Subduction factory 2. Are intermediate-depth earthquakes in subducting slabs linked to metamorphic dehydration reactions? *J. Geophys. Res.: Solid Earth* **108**, (2003).
- Ogawa, M. Shear instability in a viscoelastic material as the cause of deep focus earthquakes. *J. Geophys. Res.: Solid Earth* **92**, 13801–13810 (1987).
- Kelemen, P. B. & Hirth, G. A periodic shear-heating mechanism for intermediate-depth earthquakes in the mantle. *Nature* **446**, 787–790 (2007).
- Zhang, H. et al. High-resolution subducting-slab structure beneath northern Honshu, Japan, revealed by double-difference tomography. *Geology* **32**, 361–364 (2004).
- Sippl, C., Schurr, B., Asch, G. & Kummerow, J. Seismicity structure of the northern Chile forearc from > 100,000 double-difference relocated hypocenters. *J. Geophys. Res.: Solid Earth* **123**, 4063–4087 (2018).
- Derode, B. & Campos, J. Energy budget of intermediate-depth earthquakes in northern Chile: Comparison with shallow earthquakes and implications of rupture velocity models used. *Geophys. Res. Lett.* **46**, 2484–2493 (2019).
- Kuge K., Kase Y., Urata Y., Campos J., Perez A. Rupture characteristics of the 2005 Tarapaca, northern Chile, intermediate-depth earthquake: Evidence for heterogeneous fluid distribution across the subducting oceanic plate? *J. Geophys. Res.: Solid Earth* **115**, (2010).
- Cabrera, L. et al. Northern Chile intermediate-depth earthquakes controlled by plate hydration. *Geophys. J. Int.* **226**, 78–90 (2021).
- Kausel, E. & Campos, J. The Ms= 8 tensional earthquake of 9 December 1950 of northern Chile and its relation to the seismic potential of the region. *Phys. Earth Planet. Inter.* **72**, 220–235 (1992).
- Delouis B., Legrand D. Mw 7.8 Tarapaca intermediate depth earthquake of 13 June 2005 (northern Chile): Fault plane identification and slip distribution by waveform inversion. *Geophys. Res. Lett.* **34**, (2007).
- Peyrat, S. & Favreau, P. Kinematic and spontaneous rupture models of the 2005 Tarapacá intermediate depth earthquake. *Geophys. J. Int.* **181**, 369–381 (2010).
- Chu, S. & Beroza, G. Aftershock productivity of intermediate-depth earthquakes in Japan. *Geophys. J. Int.* **230**, 448–463 (2022).
- Wimpenny, S., Craig, T. & Marcou, S. Re-examining temporal variations in intermediate-depth seismicity. *J. Geophys. Res.: Solid Earth* **128**, e2022JB026269 (2023).
- Herrera, C. et al. Rupture properties of the 2020 M w 6.8 Calama (northern Chile) intraslab earthquake. Comparison with similar intraslab events in the region. *Geophys. J. Int.* **232**, 2070–2079 (2023).
- Contreras-Reyes, E. et al. Subduction zone fluids and arc magmas conducted by lithospheric deformed regions beneath the central Andes. *Sci. Rep.* **11**, 23078 (2021).
- Jia, Z. et al. The 2018 Fiji Mw 8.2 and 7.9 deep earthquakes: One doublet in two slabs. *Earth Planet. Sci. Lett.* **531**, 115997 (2020).
- Jia, Z., Wang, X. & Zhan, Z. Multifault models of the 2019 Ridgecrest sequence highlight complementary slip and fault junction instability. *Geophys. Res. Lett.* **47**, e2020GL089802 (2020).
- Jia, Z., Zhan, Z. & Kanamori, H. The 2021 south Sandwich Island Mw 8.2 Earthquake: A slow event sandwiched between regular ruptures. *Geophys. Res. Lett.* **49**, e2021GL097104 (2022).
- Potin, B., Ruiz, S., Aden-Antoniow, F., Madariaga, R. & Barrientos, S. A Revised Chilean Seismic Catalog from 1982 to Mid-2020. *Seismol. Res. Lett.* **96**, 484–498 (2025).
- Hartzell, S. H. Earthquake aftershocks as Green's functions. *Geophys. Res. Lett.* **5**, 1–4 (1978).
- Dreger, D. Empirical Green's function study of the January 17, 1994 Northridge, California earthquake. *Geophys. Res. Lett.* **21**, 2633–2636 (1994).
- Mueller, C. S. Source pulse enhancement by deconvolution of an empirical Green's function. *Geophys. Res. Lett.* **12**, 33–36 (1985).
- Velasco, A. A., Ammon, C. J. & Lay, T. Empirical green function deconvolution of broadband surface waves: Rupture directivity of the 1992 Landers, California (Mw= 7.3), earthquake. *Bull. Seismol. Soc. Am.* **84**, 735–750 (1994).
- Park, S. & Ishii, M. Inversion for rupture properties based upon 3-D directivity effect and application to deep earthquakes in the Sea of Okhotsk region. *Geophys. J. Int.* **203**, 1011–1025 (2015).
- He, X. & Ni, S. Rapid rupture directivity determination of moderate dip-slip earthquakes with teleseismic body waves assuming reduced finite source approximation. *J. Geophys. Res.: Solid Earth* **122**, 5344–5368 (2017).
- Zhan, Z., Helberger, D. V., Kanamori, H. & Shearer, P. M. Super-shear rupture in a M w 6.7 aftershock of the 2013 Sea of Okhotsk earthquake. *Science* **345**, 204–207 (2014).
- Yamasaki T., Seno T. Double seismic zone and dehydration embrittlement of the subducting slab. *J. Geophys. Res. Solid Earth* **108**, (2003).

40. Sime, N., Wilson, C. R. & van Keken, P. E. Thermal modeling of subduction zones with prescribed and evolving 2D and 3D slab geometries. *Prog. Earth Planet. Sci.* **11**, 14 (2024).
41. Hayes, G. P. et al. Slab2, a comprehensive subduction zone geometry model. *Science* **362**, 58–61 (2018).
42. Wada I., Wang K. Common depth of slab-mantle decoupling: Reconciling diversity and uniformity of subduction zones. *Geochim. Geophys. Geosyst.* **10**, (2009).
43. van Keken, P. E. & Wilson, C. R. An introductory review of the thermal structure of subduction zones: III—Comparison between models and observations. *Prog. Earth Planet. Sci.* **10**, 57 (2023).
44. Ferrand, T. P. & Manea, E. F. Dehydration-induced earthquakes identified in a subducted oceanic slab beneath Vrancea, Romania. *Sci. Rep.* **11**, 10315 (2021).
45. Schmidt, M. W. & Poli, S. Experimentally based water budgets for dehydrating slabs and consequences for arc magma generation. *Earth Planet. Sci. Lett.* **163**, 361–379 (1998).
46. Ferrand, T. P. et al. Dehydration-driven stress transfer triggers intermediate-depth earthquakes. *Nat. Commun.* **8**, 15247 (2017).
47. Kanamori, H., Anderson, D. L. & Heaton, T. H. Frictional melting during the rupture of the 1994 Bolivian earthquake. *Science* **279**, 839–842 (1998).
48. Zhan, Z., Kanamori, H., Tsai, V. C., Helmberger, D. V. & Wei, S. Rupture complexity of the 1994 Bolivia and 2013 Sea of Okhotsk deep earthquakes. *Earth Planet. Sci. Lett.* **385**, 89–96 (2014).
49. Tibi R., Bock G., Wiens D. A. Source characteristics of large deep earthquakes: Constraint on the faulting mechanism at great depths. *J. Geophys. Res.: Solid Earth* **108**, (2003).
50. Ide, S. & Takeo, M. The dynamic rupture process of the 1993 Kushiro-oki earthquake. *J. Geophys. Res.: Solid Earth* **101**, 5661–5675 (1996).
51. Li, S., Moreno, M., Bedford, J., Rosenau, M. & Oncken, O. Revisiting viscoelastic effects on interseismic deformation and locking degree: A case study of the Peru-North Chile subduction zone. *J. Geophys. Res.: Solid Earth* **120**, 4522–4538 (2015).
52. Prieto, G. A. et al. Seismic evidence for thermal runaway during intermediate-depth earthquake rupture. *Geophys. Res. Lett.* **40**, 6064–6068 (2013).
53. Poli, P., Prieto, G., Rivera, E. & Ruiz, S. Earthquakes initiation and thermal shear instability in the Hindu Kush intermediate depth nest. *Geophys. Res. Lett.* **43**, 1537–1542 (2016).
54. Jia, Z., Fan, W., Mao, W., Shearer, P. M. & May, D. A. Dual mechanism transition controls rupture development of large deep earthquakes. *AGU Adv.* **6**, e2025AV001701 (2025).
55. Tibi, R., Bock, G. & Estabrook, C. H. Seismic body wave constraint on mechanisms of intermediate-depth earthquakes. *J. Geophys. Res.: Solid Earth* **107**, ESE 1-1–ESE 1-23 (2002).
56. Warren L. M., Langstaff M. A., Silver P. G. Fault plane orientations of intermediate-depth earthquakes in the Middle America Trench. *J. Geophys. Res.: Solid Earth* **113**, (2008).
57. Warren, L. M., Baluyut, E. C., Osburg, T., Lisac, K. & Kokkinen, S. Fault plane orientations of intermediate-depth and deep-focus earthquakes in the Japan-Kuril-Kamchatka subduction zone. *J. Geophys. Res.: Solid Earth* **120**, 8366–8382 (2015).
58. Vallée M., Dunham E. M. Observation of far-field Mach waves generated by the 2001 Kokoxili supershear earthquake. *Geophys. Res. Lett.* **39**, (2012).
59. Bao, H. et al. Early and persistent supershear rupture of the 2018 magnitude 7.5 Palu earthquake. *Nat. Geosci.* **12**, 200–205 (2019).
60. Andrews, D. Rupture propagation with finite stress in antiplane strain. *J. Geophys. Res.* **81**, 3575–3582 (1976).
61. Broberg K. B. *Cracks and fracture*. Elsevier (1999).
62. Liu, Y. & Lapusta, N. Transition of mode II cracks from sub-Rayleigh to intersonic speeds in the presence of favorable heterogeneity. *J. Mech. Phys. Solids* **56**, 25–50 (2008).
63. Hill, D. P. et al. Seismicity remotely triggered by the magnitude 7.3 Landers, California, earthquake. *Science* **260**, 1617–1623 (1993).
64. Gomberg, J., Reasenberg, P., Bodin, P. L. & Harris, R. Earthquake triggering by seismic waves following the Landers and Hector Mine earthquakes. *Nature* **411**, 462–466 (2001).
65. Velasco, A. A., Hernandez, S., Parsons, T. & Pankow, K. Global ubiquity of dynamic earthquake triggering. *Nat. Geosci.* **1**, 375–379 (2008).
66. Luo, Y. & Wiens, D. A. High rates of deep earthquake dynamic triggering in the thermal halos of subducting slabs. *Geophys. Res. Lett.* **47**, e2019GL086125 (2020).
67. Li, J., Kim, T., Lapusta, N., Biondi, E. & Zhan, Z. The break of earthquake asperities imaged by distributed acoustic sensing. *Nature* **620**, 800–806 (2023).
68. Beroza, G. C. & Mikumo, T. Short slip duration in dynamic rupture in the presence of heterogeneous fault properties. *J. Geophys. Res.: Solid Earth* **101**, 22449–22460 (1996).
69. Dunham, E. M., Favreau, P. & Carlson, J. A supershear transition mechanism for cracks. *Science* **299**, 1557–1559 (2003).
70. Gibbons, S. J. & Ringdal, F. The detection of low magnitude seismic events using array-based waveform correlation. *Geophys. J. Int.* **165**, 149–166 (2006).
71. Beaucé, E., Frank, W. B. & Romanenko, A. Fast matched filter (FMF): An efficient seismic matched-filter search for both CPU and GPU architectures. *Seismol. Res. Lett.* **89**, 165–172 (2018).
72. Husen, S., Kissling, E., Flueh, E. & Asch, G. Accurate hypocentre determination in the seismogenic zone of the subducting Nazca Plate in northern Chile using a combined on-/offshore network. *Geophys. J. Int.* **138**, 687–701 (1999).
73. Peng, Z. & Zhao, P. Migration of early aftershocks following the 2004 Parkfield earthquake. *Nat. Geosci.* **2**, 877–881 (2009).
74. Dascher-Cousineau, K., Brodsky, E. E., Lay, T. & Goebel, T. H. What controls variations in aftershock productivity?. *J. Geophys. Res.: Solid Earth* **125**, e2019JB018111 (2020).
75. Wells, D. L. & Coppersmith, K. J. New empirical relationships among magnitude, rupture length, rupture width, rupture area, and surface displacement. *Bull. Seismol. Soc. Am.* **84**, 974–1002 (1994).
76. Bodin T. et al Transdimensional inversion of receiver functions and surface wave dispersion. *J. Geophys. Res.: Solid Earth* **117**, (2012).
77. Minson, S. E. & Dreger, D. S. Stable inversions for complete moment tensors. *Geophys. J. Int.* **174**, 585–592 (2008).
78. Kikuchi, M. & Kanamori, H. Inversion of complex body waves—III. *Bull. Seismol. Soc. Am.* **81**, 2335–2350 (1991).
79. Qian, Y., Ni, S., Wei, S., Almeida, R. & Zhang, H. The effects of core-reflected waves on finite fault inversions with teleseismic body wave data. *Geophys. J. Int.* **211**, 936–951 (2017).
80. Zhu, L. & Rivera, L. A. A note on the dynamic and static displacements from a point source in multilayered media. *Geophys. J. Int.* **148**, 619–627 (2002).
81. Johnston G., Riddell A., Hausler G. The international GNSS service. *Springer handbook of global navigation satellite systems*, 967–982 (2017).
82. González-Vidal, D. et al. Relation between oceanic plate structure, patterns of interplate locking and microseismicity in the 1922 Atacama seismic gap. *Geophys. Res. Lett.* **50**, e2023GL103565 (2023).
83. Klotz J. et al. IPOC cGPS-continuous mode GPS data in the IPOC Region, Northern Chile. (2017).
84. Báez, J. C. et al. The Chilean GNSS network: Current status and progress toward early warning applications. *Seismol. Res. Lett.* **89**, 1546–1554 (2018).
85. Dach R. *Bernese GNSS Software Version 5.2. User manual/Publikation Digital AG*, (2015).
86. Altamimi, Z., Rebischung, P., Collilieux, X., Métivier, L. & Chanard, K. ITRF2020: an augmented reference frame refining the modeling of nonlinear station motions. *J. Geod.* **97**, 47 (2023).

87. Nikkhoo, M. & Walter, T. R. Triangular dislocation: an analytical, artefact-free solution. *Geophys. J. Int.* **201**, 1119–1141 (2015).
88. Ortega-Culaciati, F., Simons, M., Ruiz, J., Rivera, L. & Díaz-Salazar, N. An epic Tikhonov regularization: Application to quasi-static fault slip inversion. *J. Geophys. Res.: Solid Earth* **126**, e2020JB021141 (2021).
89. Diamond, S. & Boyd, S. CVXPY: A Python-embedded modeling language for convex optimization. *J. Mach. Learn. Res.* **17**, 1–5 (2016).
90. Hutko, A. R. et al. Data products at the IRIS-DMC: Growth and usage. *Seismol. Res. Lett.* **88**, 892–903 (2017).
91. Stein, C. A. & Stein, S. A model for the global variation in oceanic depth and heat flow with lithospheric age. *Nature* **359**, 123–129 (1992).
92. Seton, M. et al. Global continental and ocean basin reconstructions since 200. *MA Earth-Sci. Rev.* **113**, 212–270 (2012).
93. Turcotte D. L., Schubert G. *Geodynamics*. Cambridge University Press (2002).
94. Katsura, T., Yoneda, A., Yamazaki, D., Yoshino, T. & Ito, E. Adiabatic temperature profile in the mantle. *Phys. Earth Planet. Inter.* **183**, 212–218 (2010).

## Acknowledgements

IRIS Data Services, including the Data Management Center, and data from the National Seismological Center (CSN) of the University of Chile were used for access to seismic waveforms recorded by global seismic networks II, IU, IC, G, GT, PS, the CSN strong motion and GNSS networks, the related metadata, and/or derived products used in this study. TWB was partially supported by NSF EAR 2121666 and 1925939. SR & JCB would like to thank for the support of the FONDECYT Regular project N°1240501, ANID, Chile. MM was supported by FONDECYT 1221507 and UC Open Seed Fund 2023 project (198). WM is supported by the Fundamental Research Funds for the Central Universities. BP and SR thank the Programa de Riesgo Sísmico (PRS) of the Universidad de Chile. MCF acknowledges support from ANID, Chile, through the Doctorado Nacional scholarship N°2024-21241960. ZJ was supported by UTIG's startup funding and Bluesky program funding. We thank Jorge Crempien for handling the customs process for the equipment. Our thermal model calculations were performed on the Anvil computer at Purdue University, supported by the NSF.

## Author contributions

Z.J. conceptualized and led the study, performed the subevent inversion and source time deconvolutions, and wrote the initial draft of the manuscript. W.M. performed the thermal simulations. M.C.F. and S.R. performed seismicity detection and relocation. S.B., M.M., and J.C.B.

performed the geodetic slip inversions. TWB performed forward deformation analyses and coordinated the collaboration. B.P. provided the refined slab interface model and background seismicity. D.C. and L.C. performed the earthquake detection using template matching. M.M., T.W.B., S.R., W.M., J.C.B., D.C., and L.C. provided comments on the results. All authors contributed to writing the final manuscript.

## Competing interests

Authors declare no competing interests.

## Additional information

**Supplementary information** The online version contains supplementary material available at <https://doi.org/10.1038/s41467-025-63480-5>.

**Correspondence** and requests for materials should be addressed to Zhe Jia.

**Peer review information** *Nature Communications* thanks Yong Zheng, and the other, anonymous, reviewer(s) for their contribution to the peer review of this work. A peer review file is available.

**Reprints and permissions information** is available at <http://www.nature.com/reprints>

**Publisher's note** Springer Nature remains neutral with regard to jurisdictional claims in published maps and institutional affiliations.

**Open Access** This article is licensed under a Creative Commons Attribution-NonCommercial-NoDerivatives 4.0 International License, which permits any non-commercial use, sharing, distribution and reproduction in any medium or format, as long as you give appropriate credit to the original author(s) and the source, provide a link to the Creative Commons licence, and indicate if you modified the licensed material. You do not have permission under this licence to share adapted material derived from this article or parts of it. The images or other third party material in this article are included in the article's Creative Commons licence, unless indicated otherwise in a credit line to the material. If material is not included in the article's Creative Commons licence and your intended use is not permitted by statutory regulation or exceeds the permitted use, you will need to obtain permission directly from the copyright holder. To view a copy of this licence, visit <http://creativecommons.org/licenses/by-nc-nd/4.0/>.

© The Author(s) 2025